

Electroless plating synthesis of bifunctional crystalline/amorphous Pd-NiFeB heterostructure catalysts for boosted electrocatalytic water splitting

Bowen Lu ^{a,b}, Rongmin Dun ^a, Wei Wang ^{a,*}, Jian Huang ^a, Jingxian Wu ^{a,b}, Zile Hua ^{a,b,**}, Jianlin Shi ^{a,b}

^a State Key Laboratory of High Performance Ceramics and Superfine Microstructure, Shanghai Institute of Ceramics Chinese Academy of Sciences, 1295 Dingxi Road, Shanghai, China

^b Centre of Materials Science and Optoelectronics Engineering, University of Chinese Academy of Sciences, Beijing, China



ARTICLE INFO

Keywords:

Electroless plating
Amorphous-crystalline heterostructure
Bifunctional
Electrocatalytic water splitting

ABSTRACT

The rational design of low-cost and high-efficient electrocatalysts to overcome the energy barrier of water splitting has aroused great attentions. The amorphous-crystalline interface heterostructure has been verified to be a promising design for modulating the charge redistribution at interface active sites for promoting water splitting, which, however, remains a challenge. Herein, a bifunctional electrocatalyst with amorphous-crystalline heterostructures is fabricated by hybridizing amorphous NiFeB alloy and crystalline Pd nanoclusters on the nickel foam (NF) via a simple electroless plating strategy. The as-synthesized Pd-NiFeB/NF catalyst exhibits excellent HER and OER performance. Moreover, the assembled Pd-NiFeB/NF//Pd-NiFeB/NF electrolytic system requires a rather low cell voltage of 1.81 V to drive the durable current density of 500 mA cm^{-2} for at least 100 h. Theoretical calculations reveal that the addition of Pd nanoclusters reduces the energy barriers for both HER and OER, which is due to the enhanced charge transfer and optimal adsorption of intermediates.

1. Introduction

With the rapid fossil fuel consumption and large emission of CO_2 , the aggravation of the greenhouse effect has led to serious environmental problems, i.e. global warming and climate change [1]. Hydrogen energy, due to its high energy density, cleanness, abundance in sources, and sustainability, is deemed to be one of the ideal and promising substitutes for traditional fossil energy [2]. Among the many hydrogen production technologies, electrochemical water splitting as a “zero emission” of CO_2 process and complementation to the intermittent wind and solar energy systems attracts great interest from both industry and academia in recent years [3]. Unfortunately, electrochemical water splitting consists of two half-reactions with high energy barriers that seriously suppress the occurrence of hydrogen evolution reaction (HER) at the cathode and the four-electron oxygen evolution reaction (OER) at the anode [4]. As a result, high overpotential is inevitably required, resulting in the increase of electrical energy consumption. Currently,

noble metal catalysts (RuO_2 , IrO_2 , or Pt) with inherent high activity are adopted to reduce the HER/OER overpotentials during water splitting [5]. However, the high cost and scarcity of noble metal components hinder their extensive deployment [6]. Therefore, it is urgent to explore a rational strategy for significantly decreasing the usage of noble metals or completely replacing them and constructing new types of low-cost and comparable or even superior catalysts.

Over the last decade, many new kinds of transition metal-based catalysts have been designed and synthesized for electrochemical water splitting, such as sulfides, [7] borides, [8] phosphides, [9] amorphous metal alloys and so on [10,11]. Compared to their crystalline counterparts, amorphous materials often exhibit more interesting electrocatalytic performance benefiting from their abundant surface dangling bonds and unsaturated coordination sites [12]. Unfortunately, the existence of large number of defects in amorphous electrocatalysts also leads to a complex route for electron moving, resulting in a high charge transfer resistance during electrocatalytic reactions [13]. To

* Corresponding author.

** Corresponding author at: State Key Laboratory of High Performance Ceramics and Superfine Microstructure, Shanghai Institute of Ceramics Chinese Academy of Sciences, 1295 Dingxi Road, Shanghai, China.

E-mail addresses: wangwei1@mail.sic.ac.cn (W. Wang), huazl@mail.sic.ac.cn (Z. Hua).

solve this problem with amorphous electrocatalysts, recently new amorphous-crystalline (*a-c*) heterostructure catalysts have been developed and verified as an efficient measure by modulating the electronic structure of active sites [14]. Till now, the complex processes or harsh conditions are always required for synthesis of *a-c* heterostructure catalysts and in most cases, only the sole function, e.g. HER or OER activity, have been endowed [15–17]. Thus, there is a need for application-oriented *a-c* heterostructure catalysts with a facile synthesis process that can enable both HER and OER bifunctionality for electrochemical water splitting.

Benefiting from the smooth surface reconstruction during OER and accordingly the formation of high-valence metal oxyhydroxides as real active species, NiFe-based materials is one of good candidates for high performance non-precious metal electrocatalyst [18,19]. However, their HER performance is still unsatisfactory. Palladium (Pd) element plays a critical role in modern fine chemical and petrochemical industries, and Pd-based catalysts also show great potential in electrochemistry fields, especially towards HER [20,21]. Moreover, because of the electron coupling between Pd species and matrices, the electronic structure and consequently electrocatalytic properties of composites could be modulated. Rafael et al. ever synthesized Pd nanoclusters incorporated Ni (OH)₂ which exhibited not only the expected HER catalytic activity, but also the enhanced anode ethanol oxidation capability and stability due to their synergistic effect [22]. However, few reports about Pd-containing HER and OER bifunctional electrocatalysts could be found [23].

Herein, based on the facile electroless plating strategy, a new kind of amorphous NiFeB alloy and crystalline Pd nanoclusters heterostructure electrocatalysts (Pd-NiFeB) have been formed on the nickel foam (NF) for the first time. Materials synthesis by electroless plating is a redox reaction process. Generally, it can be accomplished in a short time of several hours under atmosphere pressure and relatively low temperature, which reduce the energy consumption for materials preparation and possessing the advantage of easy manipulation. Owing to the electronegativity difference between Pd and Ni species, electron transfer and charge redistribution occur in the resultant Pd-NiFeB catalysts. Benefiting from the optimized d-band center and enhanced charge transfer rate, it exhibits outstanding electrocatalytic performances for both HER and OER in alkaline electrolytes of 1.0 M KOH. Furthermore, the assembled two-electrode water splitting electrolyzer displays superb electrocatalytic performances with an ultralow cell voltage of 1.81 V at the current density of 500 mA cm⁻² and negligible decays after a 100-h durability test. Operando Raman spectra and density functional theory (DFT) calculations further confirms the dual functions of Pd species in the synthesized Pd-NiFeB heterostructure catalysts. During OER process, it is an effective promoting agent for the formation of high valence Ni species on the anode. As for HER process, it can accelerate the dissociation of water to enhance the HER catalytic activity. This work is a guide to practically fabricate high-effective and low-cost heterostructure electrocatalysts for electrochemical water splitting.

2. Experimental section

2.1. Materials

Nickel sulfate (NiSO₄·6H₂O), ferrous sulfate heptahydrate (FeSO₄·7H₂O), sodium tetrachloropalladate (Na₂PdCl₄), dimethylamine borane (DMAB), ethylenediamine (C₂H₈N₂, EDA), ammonium sulfate ((NH₄)₂SO₄), sodium citrate (C₆H₅Na₃O₇), hydrochloric acid (HCl) and potassium hydroxide (KOH) were purchased from Sigma-Aldrich and Adamas. All chemicals are of analytical grade and were used without any further purification. Nickel foam (NF) was purchased from the SaiBo Electrochemical Materials Co., Ltd.

2.2. Synthesis of Pd-NiFeB/NF electrode

In the first place, nickel foam (NF) was cleaned with HCl and deionized water to remove the organic materials or impurities of surface. Subsequent, one piece of pretreated NF was immersed into a 200 mL freshly prepared electroless plating solution containing NiSO₄·6 H₂O (0.05 mol/L), FeSO₄·7 H₂O (0.05 mol/L), Na₂PdCl₄ (0.01 mmol/L), C₂H₈N₂ (0.03 mol/L), (NH₄)₂SO₄ (0.5 mol/L), C₆H₅Na₃O₇ (0.1 mol/L), and DMAB (0.03 mol/L). Then, the electroless plating solution was heated for 2 h at 40 °C. After 2 h of reaction, the as-synthesized Pd-NiFeB/NF was washed with deionized water and dried overnight. The NiFeB/NF, NiB/NF, and PdB/NF were fabricated by similar processes without Pd, Fe and Pd, Ni and Fe source, respectively. Moreover, the detailed synthesis process of Pt/C/NF and IrO₂/NF electrode was shown in Supporting Information (SI).

2.3. Physical characterizations

A scanning electron microscopy (SEM, Japan S-4800) and transmission electron microscopy (TEM, FEI-Talos F200X) was applied to analyse the morphology and microstructure of the catalysts. The crystallographic and compositional information were obtained from the Powder X-ray diffraction (XRD, Bruker D8-Advance with Cu K α radiation). X-ray photoelectron spectroscopy (XPS, EscaLab 250Xi) was performed to investigate the chemical composition and state of catalysts. Inductively coupled plasma optical emission spectroscopy (ICP-OES) analysis was carried out with a VARIAN 710ES system. Raman spectra were collected on a LabRAM HR Evolution Lab-HRDL 20 system equipped with a 532-nm laser.

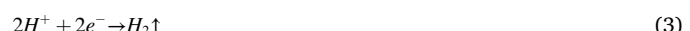
2.4. Electrochemical measurements

The details of the electrochemical measurements involved in the experiment are provided in the SI.

3. Results and discussion

3.1. Material synthesis and characterization

As illustrated in Fig. 1a, the electrocatalysts were fabricated on NF via a facile electroless plating method. According to the redox mechanism, during this process, the oxidation of dimethylaminoborane ((CH₃)₂NH·BH₃, DMAB) and the release of electrons would be firstly occurred as Eq. (1) [24].



Then, metal ions, i.e. Ni²⁺, Fe²⁺ and Pd²⁺, and hydrogen ions would be reduced by the generated electrons (Eq. (2) and (3)) to the metals (M⁰) and hydrogen gas (H₂), respectively. At last, the resulting zero-valent Ni⁰/Fe⁰ and B⁰ would mix to form the metal-B alloys, e.g. NiB and NiFeB. The detailed synthesis conditions and materials characterization could be found in the Experimental Section and SI. Phase structures of as-prepared materials (denoted as PdB/NF, NiFeB/NF, and Pd-NiFeB/NF) were identified by powder X-ray diffraction (XRD). In Fig. S1 (SI), all XRD patterns show the same group of diffraction peaks at 2theta of 44.5°, 51.8°, and 76.3°, which are attributed to the (111), (200), and (220) planes of Ni metal substrate (JCPDS70–1849), respectively. Therefore, to eliminate the interference of high-intensity diffraction peaks of NF matrix, the catalyst layers were peeled off and characterized. As shown in Fig. 1b, for all powder samples, only an

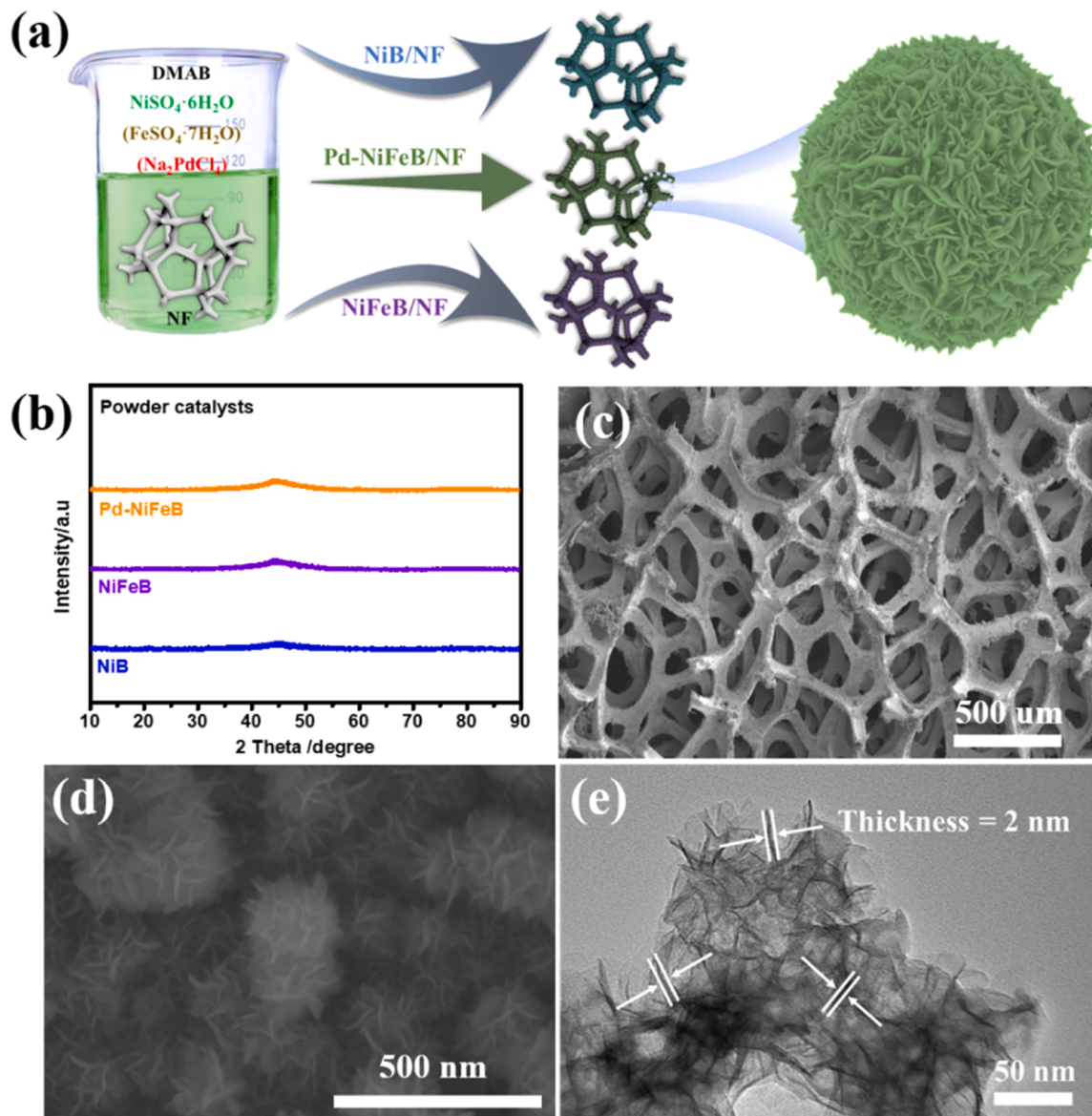


Fig. 1. (a) Schematic illustration of electroless plating process for materials preparation. (b) XRD patterns of synthesized powder materials. (c, d) SEM images of sample Pd-NiFeB/NF and (e) TEM image of scratched Pd-NiFeB powders.

indiscernible broad diffraction peak appears at 2theta of around 45°, indicating the amorphous nature of synthesized NiB and NiFeB alloy,

which is consistent with previous reports [25]. Under similar electroless plating conditions, although sample PdB/NF displays the distinct characteristic peaks at 2theta of 39.4°, 48.5°, 66.8°, and 80.4° ascribed to the (111), (200), (220), and (311) planes of the face-centered cubic structure of metal Pd (JCPDS87-0641) in Fig. S1, they are absent for sample Pd-NiFeB/NF and powder Pd-NiFeB. The possible reason lies in the relatively low concentration and small particle size of Pd species in it, which is confirmed by the following characterization results of the inductively coupled plasma optical emission spectroscopy (ICP-OES) and transmission electron microscopy (TEM).

The micro-morphology of NF substrates and as-prepared materials was examined by scanning electron microscopy (SEM). Compared to the smooth surface of the NF substrates (Fig. S2), the synthesized Pd-NiFeB/NF electrode exhibits a rough surface, as illustrated in Fig. 1c. At higher magnification, Fig. 1d and Fig. S3 reveals that the grown catalyst layer on NF substrates is composed of submicrometer-sized pompon-like nanoparticles which are assembled by smaller-sized nanosheets with thickness of 2 nm (Fig. 1e). The similar morphological characteristics

could be found for sample NiB/NF and NiFeB/NF, as shown in Fig. S4 and Fig. S5, and the size of the unit pompon-like particles is slightly larger. This open-ended nanostructure is similar to the typical nanosheet arrays of benchmark transition metal-based layer double hydroxide (LDH) electrocatalysts featuring with their high specific surface area, convenience to the electrolyte transport and consequently superior catalytic performance [26]. However, this interesting open-ended nanostructure is scarce for previously reported P or B-reduced amorphous metal alloy self-supporting electrode, most of which comprise of dense and spherical nanometer-sized particles [27]. In a recent work, to prepare NiCoFeB nanosheet array self-supporting electrode, a two-step electrosynthesis procedure with pre-synthesized Ni-Co-Fe LDH as the sacrificing template was reported [28]. Thus, considering the simplicity and mild synthesis conditions of the electroless plating method, high performance and potential applications of here reported (Pd-)NiFeB/NF electrocatalysts are expected. Fig. S6 are the SEM image and corresponding elemental mapping of as-synthesized Pd-NiFeB/NF, demonstrating the homogeneous distribution of Ni, Fe, B and Pd species throughout the whole samples. The quantitative analysis results, obtained from both SEM/EDS and ICP-OES, are summarized in Table S1

and Table S2, presenting the consistent chemical compositions. In detail, for sample Pd-NiFeB/NF, the mass fraction of Ni, Fe, B and Pd elements are 77.6 wt%, 7.3 wt%, 12.9 wt%, and 2.2 wt%, respectively. The relatively low Pd content is in accordance with above XRD results in which the characteristic diffraction peaks associated with metal Pd is undetectable.

To in-depth investigate the crystallization state of synthesized materials, the Pd-NiFeB catalyst layers were peeled off from the NF by ultrasonication and analyzed by high-resolution TEM (HRTEM). The elemental mapping images (Fig. 2a) indicate a uniform distribution on the Pd-NiFeB/NF electrode of the Ni, Fe, Pd and B elements. Being consistent with above XRD results and previous reports, most areas in HRTEM image of Fig. 2b shows the disordered atomic arrangement, i.e. Area 1, reflecting the amorphous nature of NiFeB phase. Also, the corresponding weak diffuse halo of inset selected-area electron diffraction (SAED) pattern offers the additional evidence. Meanwhile, some crystalline domains of about 2–5 nm randomly embedded in the amorphous NiFeB matrix can be identified, which are marked with green areas (Area 2), as shown in Fig. 2b. At higher magnification, the lattice fringe is clearer (Fig. 2c) and the line scan of the HRTEM image was extracted with digital micrograph software, as shown in Figure 2C1. The calculated interplanar spacing is 0.227 nm, matching with the (111) plane of metallic Pd. In a word, all above results confirm the formation of amorphous NiFeB alloy - crystalline Pd nanoclusters heterostructure in the synthesized Pd-NiFeB materials.

To systematically characterize the element composition and chemical valence of synthesized materials by the electroless plating method, X-ray photoelectron spectroscopy (XPS) profiles with depth were obtained through argon ion etching with varied times (30–180 s). As shown in Fig. 3a, the XPS spectrum of Ni 2p for sample Pd-NiFeB/NF free from the argon-ion etching reveals the co-existence of Ni⁰ and Ni²⁺/³⁺ species in the materials surface. After 30 s of argon ion etching (about 2 nm in depth), the valence state of Ni species undergoes a significant

transition from a oxidation state Ni²⁺/Ni³⁺ to the metallic Ni⁰ and keeps the absolute dominance with further etching, illustrating the Ni⁰ as the main component in the synthesized materials [29,30]. And, the XPS depth spectra of Fe 2p also exhibits similar trends as those of Ni 2p (Fig. S7). In Fig. 3b, B 1s spectra of synthesized Pd-NiFeB/NF materials show that the peaks at binding energies of 188.13 and 191.85 eV are assigned to metal-B (M-B) bond and borate (B-O), respectively [31]. Meanwhile, as the etching depth increases, the B 1s depth spectra show the gradual decline of B-O peak and the increased M-B peak intensity, further confirming the formation of metal-B alloy in the bulk of synthesized materials, as illustrated in Eqs. (1) - (4). The presence of high-valent Ni²⁺/Ni³⁺ species and B-O bond in the surface layer is possibly due to the oxidation in the air [11,32]. Correspondingly, the O 1s depth profiles exhibit a decreasing peak intensity with the extended argon ion etching in the Pd-NiFeB/NF (Fig. 3c). Besides, the Pd 3d spectra reveal the presence of metallic Pd (Pd⁰) with binding energy of 335.67 eV, which is consistent with above HRTEM results (Fig. 3d) [33, 34]. Further, The charge redistribution in Pd-NiFeB/NF catalyst was also noticed. Compared to the Ni 2p depth spectra of NiFeB/NF, as shown in Fig. 3e, the introduction of Pd species for sample Pd-NiFeB/NF leads to a positive shift of 0.2 eV for the binding energy of Ni⁰ from 852.91 eV to 853.11 eV. Accordingly, compared to that of sample PdB/NF (Fig. 3f), the binding energy of Pd⁰ for sample Pd-NiFeB/NF displays a negative shift of about 0.2 eV, indicating the electron transfer between Pd nanoclusters and NiFeB matrix. However, Fig. S7 and Fig. S8a show a slight difference (about 0.03 eV) for the binding energy of Fe⁰ in Pd-NiFeB/NF and NiFeB/NF samples. Thus, the above results demonstrate that the element Pd has more influence on the charge configuration around Ni atoms. Though the incorporation of element Pd does not strongly change the charge configuration around Fe atoms, the Fe species would be favourable for the activity enhancement of Ni-based electrocatalysts. Actually, in a recent work, Shannon et al. considered that when the content of Fe species was low, e.g. < 25 wt%, it would not

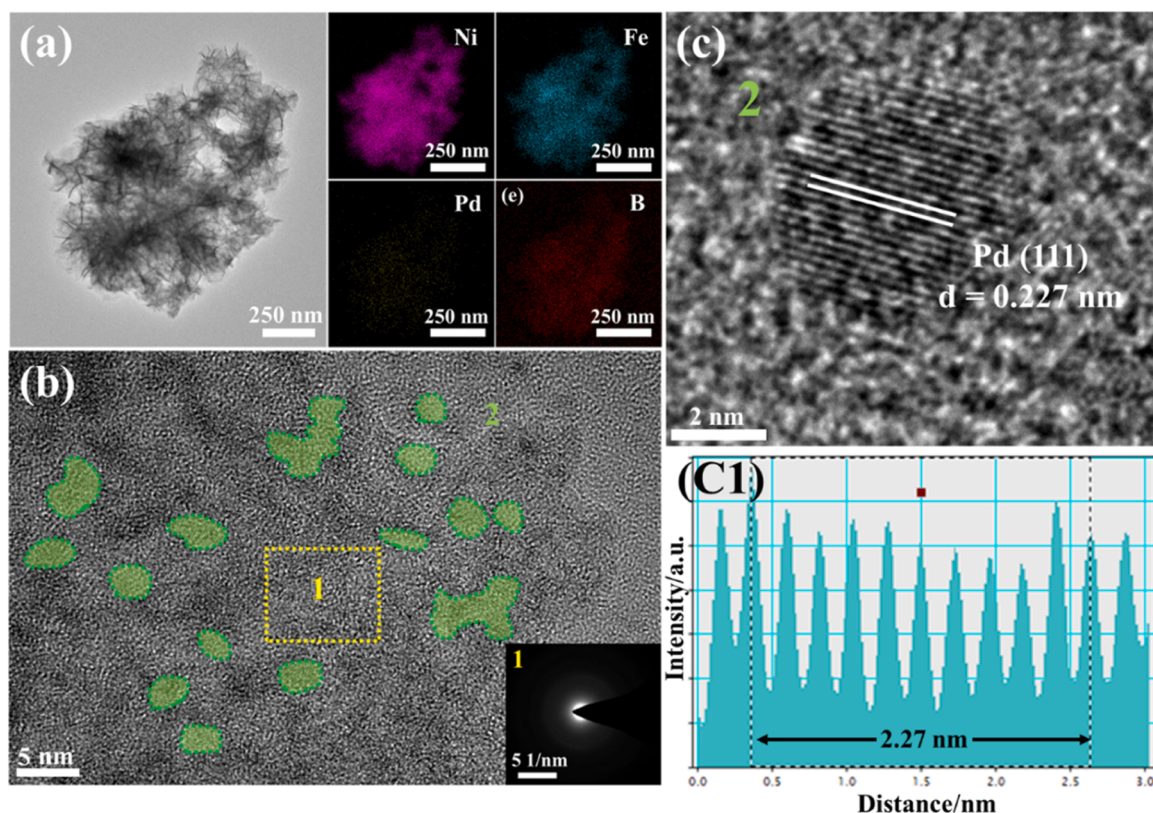


Fig. 2. (a) TEM image and the corresponding elemental mapping images of Pd-NiFeB. (b) HRTEM image of Pd-NiFeB, inset is the SAED pattern of the Area 1. (c) HRTEM image of the Area 2, (C1) Line scanning profile of the HRTEM image on the (111) plane.

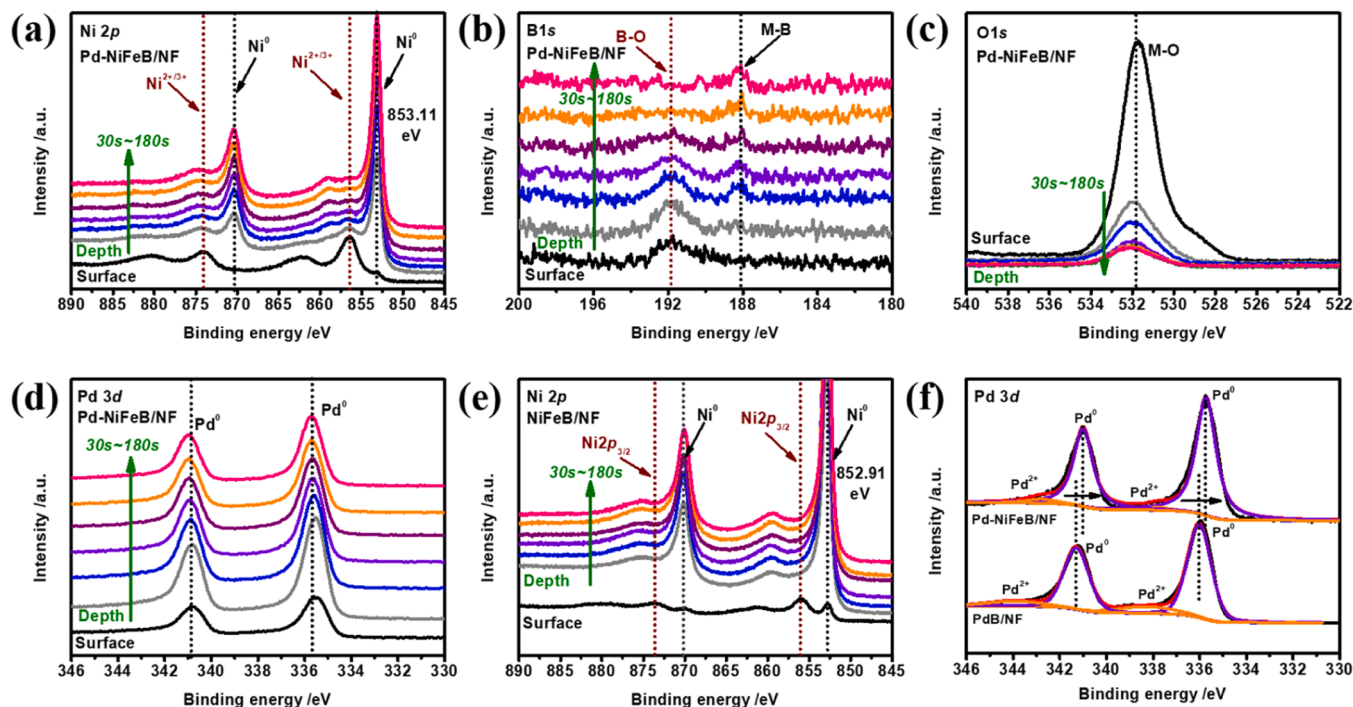


Fig. 3. XPS depth profiles of (a) Ni 2p, (b) B 1s, (c) O 1 s, and (d) Pd 3d for Pd-NiFeB/NF with varied argon ion etching time, and (e) XPS depth profiles of Ni 2p for NiFeB/NF. (f) XPS spectra of Pd 3d for Pd-NiFeB/NF and PdB/NF.

promote the further oxidation of Ni^{2+} , but could strengthen the oxidation capacity of reconstructed $\text{Ni}^{3+/4+}$ species during OER process and speed up the OER kinetics [35]. Therefore, compared to sample NiB/NF, superior OER performance is expected for sample (Pd-)NiFeB/NF.

3.2. Electrocatalytic performance analysis

The electrocatalytic performance of all samples were evaluated in 1.0 M KOH electrolyte using a standard three-electrode system. First, the linear sweep voltammetry (LSV) was examined to estimate their OER activity with a scan rate of 5 mV s^{-1} , and all tested potentials were calibrated to the reversible hydrogen electrode (RHE) with iR compensation. As shown in Fig. 4a, sample Pd-NiFeB/NF exhibits an extremely low overpotential of 270 mV at the current density of 500 mA cm^{-2} , which is not only better than NiB/NF (400 mV), NiFeB/NF (314 mV), bare NF and IrO_2/NF (Fig. S9), but also outperforms most of reported noble metal-based electrocatalysts and boride ones, as listed in Fig. 4b, reflecting its excellent OER activity [36–45]. To characterize the intrinsic catalytic activity of synthesized materials, the electrochemical surface area (ECSA) was explored based on the double-layer capacitance (C_{dl} , Fig. S10 and Fig. S11). As depicted in Fig. 4c and Fig. S11, sample Pd-NiFeB/NF exhibits the largest C_{dl} and ECSA of 29.47 mF cm^{-2} and 245.58 cm^{-2} compared with NiFeB/NF (23.84 mF cm^{-2} and 198.66 cm^{-2}), NiB/NF (15.93 mF cm^{-2} and 132.75 cm^{-2}) and the bare NF (2.98 mF cm^{-2} and 24.83 cm^{-2}), which means that sample Pd-NiFeB/NF possess more exposed active sites likely resulting from its reduced submicrometer-sized pompon-like particles and the incorporation of additional Pd species (Fig. 1d). More interestingly, the normalized polarization curve of sample Pd-NiFeB/NF, as shown in Fig. 4d, also demonstrates the highest normalized current among the synthesized catalysts, confirming its remarkable intrinsic catalytic activity.

Fig. 4e is the Tafel plots of synthesized materials and the bare NF. Apparently, sample Pd-NiFeB/NF has a smaller Tafel slope of 27.4 mV dec^{-1} than NiB/NF ($112.9 \text{ mV dec}^{-1}$), NiFeB/NF (88.6 mV dec^{-1}) and the bare NF ($141.3 \text{ mV dec}^{-1}$), indicating its faster reaction kinetics during OER. Further, to gain insight into the OER kinetics, electrochemical

impedance spectroscopy (EIS) measurements were conducted. As shown in Fig. 4f and Table S3, based on the fitting results of the equivalent circuits, the charge transfer resistance (R_{ct}) of sample Pd-NiFeB/NF is $0.4 \Omega \text{ cm}^2$, which is lower than those of NiFeB/NF ($0.8 \Omega \text{ cm}^2$), NiB/NF ($1.2 \Omega \text{ cm}^2$) and the bare NF ($2.6 \Omega \text{ cm}^2$), proving the enhanced charge transfer rate in sample Pd-NiFeB/NF. As potential high-performance catalysts, besides the activity, stability is another crucial factor. As shown in Fig. S12a, in a 100-h durability test, Pd-NiFeB/NF presents a constant current density of 500 mA cm^{-2} at the potential of 1.49 V (vs. RHE) with little fluctuation. Moreover, the difference on LSV curves is negligible between fresh and spent catalysts (Fig. S12b), confirming the high stability of synthesized Pd-NiFeB/NF.

The catalytic behavior of Pd-NiFeB/NF towards HER was also measured under the same electrolyte. As expected, due to the distinguished HER activity of Pd-based materials, sample Pd-NiFeB/NF achieves 300 mA cm^{-2} with a lower overpotential of 235 mV (Fig. 4g), which is far superior to NiFeB/NF (290 mV), and NiB/NF (330 mV). Remarkably, Pd-NiFeB/NF (249 mV) even surpasses the HER performance of Pt/C/NF benchmark at high current density of 500 mA cm^{-2} , as shown in Fig. S13. To calculate C_{dl} and ECSA of synthesized catalysts and bare NF, CV curves were measured at different scan rates (Fig. S14). The results show that sample Pd-NiFeB/NF has the largest C_{dl} (22.77 mF cm^{-2}) and ECSA (189.75 cm^{-2}) compared to those of NiFeB/NF (9.59 mF cm^{-2} and 80.91 cm^{-2}), NiB/NF (6.11 mF cm^{-2} and 50.91 cm^{-2}) and bare NF (5.31 mF cm^{-2} and 44.25 cm^{-2}), as shown in Fig. S15 and Fig. S16a. The ECSA-normalized LSV curves confirm the superior intrinsic activity of Pd-NiFeB/NF towards HER in Fig. S16b. The Tafel slope of Pd-NiFeB/NF was calculated to be 64.4 mV dec^{-1} , which is lower than NiFeB/NF ($142.1 \text{ mV dec}^{-1}$), NiB/NF ($156.3 \text{ mV dec}^{-1}$) and bare NF ($177.5 \text{ mV dec}^{-1}$) in Fig. 4h. The small Tafel slope of Pd-NiFeB/NF reveals the desired HER kinetics. Accordingly, sample Pd-NiFeB/NF also exhibits the lowest charge transfer resistance of $0.9 \Omega \text{ cm}^2$ among synthesized catalysts and bare NF, as shown in Fig. 4i and Table S4, and outstanding charge transfer capability is thus obtained. The HER stability of Pd-NiFeB/NF was tested by chronoamperometry measurement. As shown in Fig. S17, the current density almost keeps unchanged during the 100-h

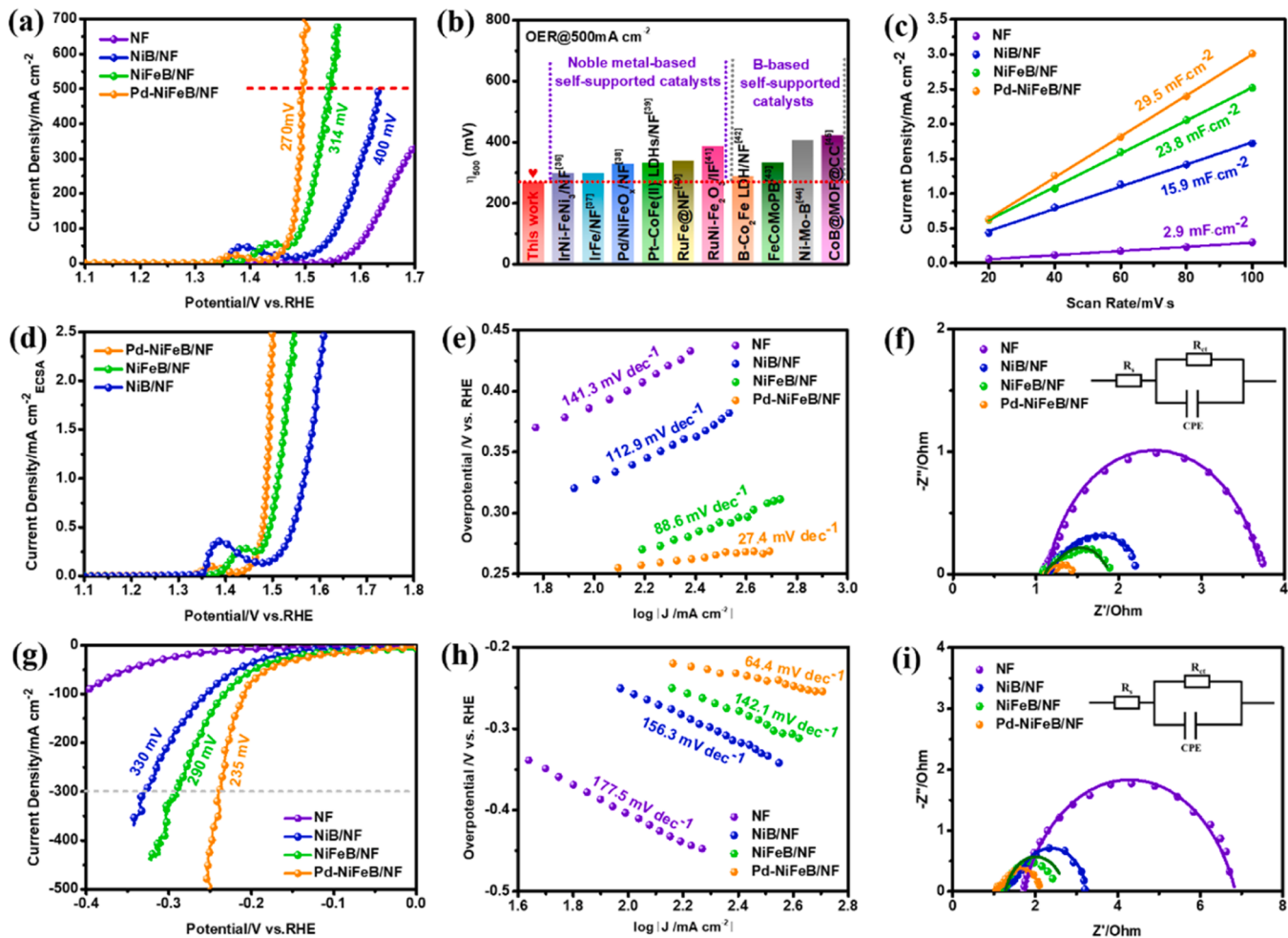


Fig. 4. Electrocatalytic OER performance for NF, NiB/NF, NiFeB/NF, and Pd-NiFeB/NF in 1.0 M KOH: (a) OER polarization curves, (b) Comparison of OER performance at current density of 500 mA cm^{-2} , (c) C_{dl} results of the as-prepared samples, (d) ECSA-normalized LSV polarization curves, (e) Tafel plots and (f) EIS Nyquist plots. HER for NF, NiB/NF, NiFeB/NF, and Pd-NiFeB/NF in 1.0 M KOH: (g) HER polarization curves, (h) Tafel plots and (i) EIS Nyquist plots.

stability test and the LSV curves before and after test are overlapped, confirming the excellent stability of synthesized Pd-NiFeB/NF towards HER in 1.0 M KOH.

Considering the superior HER and OER performances of Pd-NiFeB/NF in alkaline electrolytes, it was used as both cathode and anode for overall water splitting. As illustrated in Fig. 5a, the assembled Pd-NiFeB/NF//Pd-NiFeB/NF electrolyzer only requires a low cell voltage of 1.81 V to achieve a high current density of 500 mA cm^{-2} , significantly lower than that of NiFeB/NF (1.99 V) and NiB/NF (2.06 V). Compared to the noble metal catalysts reported in the literatures, Fig. 5b displays that here synthesized Pd-NiFeB/NF catalyst not only possesses the lowest cell voltage of 1.37 V at the current density of 10 mA cm^{-2} , but also has a relatively low Pd content of 2.2 wt%, significantly reducing the cost of the catalyst. [38,46–51] In accordance with above HER and OER electrode durability testing results, it could.

hold the constant current density of 500 mA cm^{-2} at the low cell voltage of 1.81 V for 100 h without attenuation, as shown in Fig. 5c. Moreover, in a step-cycle test, it manifests the character of quick response to the change of cell voltage from 1.65 V to 1.81 V and maintains the stable current density in each step, confirming its high stability of synthesized Pd-NiFeB/NF. The SEM and TEM characterization was performed to verify the structure and morphological change of Pd-NiFeB/NF after the 100-h durability test. As shown in Fig. S18 and Fig. S19, the Pd-NiFeB/NF materials still retains the initial submicrometer-sized pompon-like particle morphology, and Pd, Ni, Fe, and B elements keep the homogeneous distribution throughout the

whole samples. Compared to Fig. 2b of fresh Pd-NiFeB, HRTEM image of Fig. S20 shows that the amorphous NiFeB-crystalline Pd nanoclusters heterostructure keeps intact, and the lattice fringe of metal Pd nanoclusters is still clear, proving the remarkable structure stability of synthesized Pd-NiFeB catalyst. In addition, since the blocked transportation of generated H_2 or O_2 bubbles and consequently sudden burst is considered to be one of the major causes for the peeling of and even deactivation of catalyst layers, another possible reason for the excellent durability of here synthesized Pd-NiFeB/NF catalysts should be noted, which is attributed to its abundant open-ended nanostructures (Fig. 2d) favorable for the easy removal of generated H_2 bubbles from the electrode surface [52]. As shown in Fig. S21 of the digital photos of cathodes during the OER, it is obvious that few bubbles adhere to the electrode surfaces. At last, based on the comparison of the current density or voltage, it is confirmed that here synthesized Pd-NiFeB/NF catalyst has a top-ranked activity level for water splitting among the reported noble metal-based catalysts, as illustrated in Fig. 5d. [37,39,40,53–59].

3.3. Electrocatalytic mechanism

3.3.1. Operando Raman Spectra

It is well known that there exists surface reconstruction of electrocatalysts during OER reactions. To uncover the real active sites of (Pd-) NiFeB catalysts, the operando Raman spectra were collected in a relatively low KOH concentration of 0.1 M limited by the present experimental conditions. Fig. 5e and Fig. 5f demonstrate the Raman results of

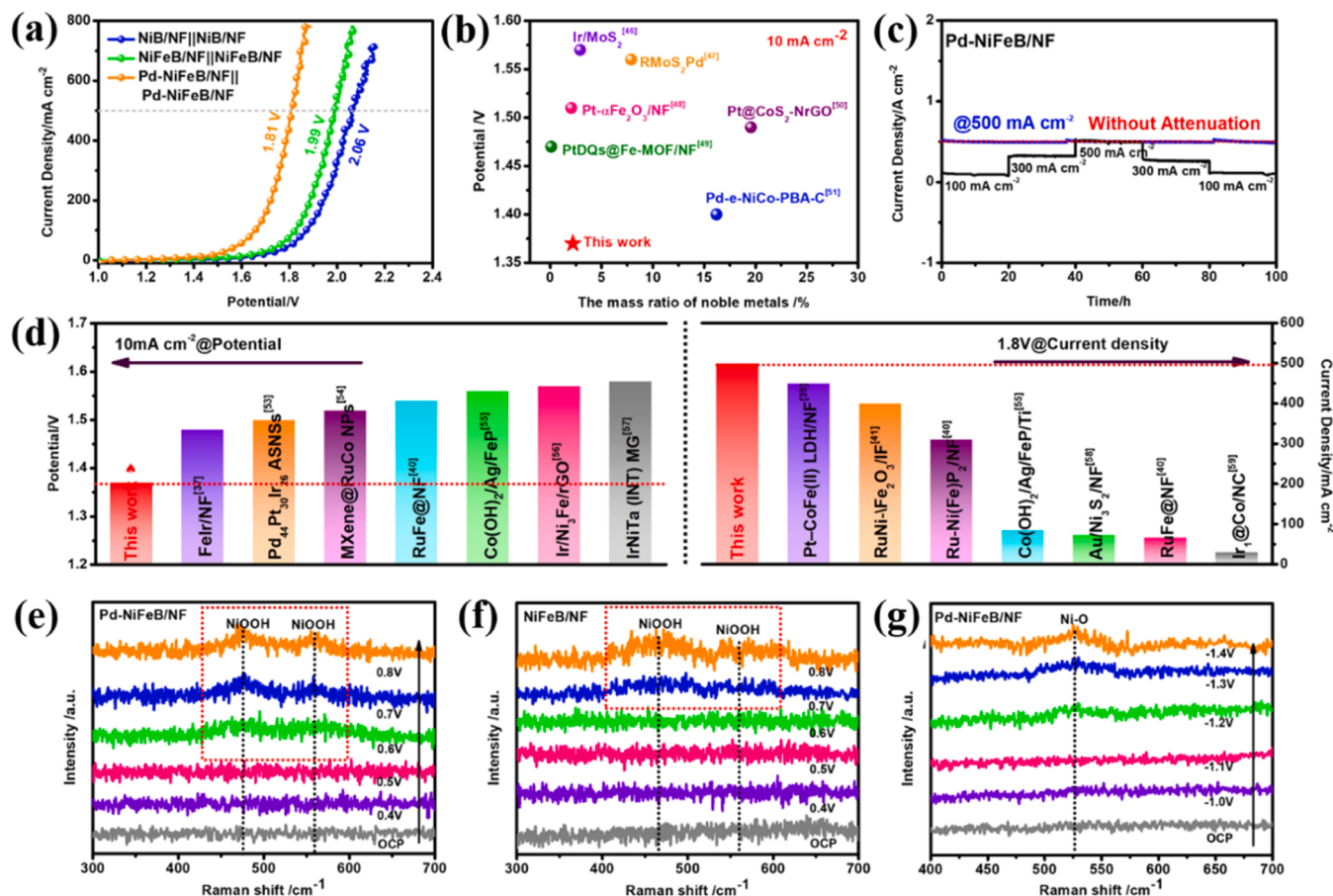


Fig. 5. (a) Polarization curves of NiB/NF||NiB/NF, NiFeB/NF||NiFeB/NF and Pd-NiFeB/NF||Pd-NiFeB/NF for overall water splitting. (b) Comparison of the potentials at 10 mA cm^{-2} between Pd-NiFeB and other reported bifunctional electrocatalysts. (c) Long-term durability test of Pd-NiFeB/NF||Pd-NiFeB/NF at 1.65 V (100 mA cm^{-2}), 1.75 V (300 mA cm^{-2}), 1.81 V (500 mA cm^{-2}) by chronoamperometry in 1.0 M KOH solution. (d) Comparison of the potentials at 10 mA cm^{-2} (left) and the current densities at 1.8 V (right). (e and f) Operando Raman spectra of NiFeB/NF and Pd-NiFeB for OER. (g) Operando Raman spectra of Pd-NiFeB for HER.

sample Pd-NiFeB/NF and NiFeB/NF with varied potentials. Apparently, there are no Raman signals detected for both of them under the open-circuit potential (OCP), illustrating that the number of active species is few. For sample Pd-NiFeB/NF, when the voltage was increased to 0.6 V, two apparent peaks appear at ~ 475 and 558 cm^{-1} , which are assigned to the stretching vibration of NiOOH. And, the oxidation peak potential of the Pd-NiFeB/NF sample is 1.45 V in 0.1 M KOH solution (Fig. S22). After the reversible hydrogen standard treatment, the potential is 0.58 V, which is consistent with that of Pd-NiFeB/NF at 0.6 V to form NiOOH. Specifically, the NiOOH represents the commonly accepted active species for OER. Moreover, the intensity of these two feature peaks becomes more pronounced with the increase of the applied voltage, reflecting the concentration increasing of active high valence Ni species. The ex-situ Raman spectra of sample Pd-NiFeB/NF experienced 100-h OER stability test offers the additional support for this conclusion, which showed the distinct stretching vibration of NiOOH at ~ 475 and 558 cm^{-1} (Fig. S23). Meanwhile, XPS spectra of spent Pd-NiFeB/NF after the 100-h OER stability test were characterized. As expected, the high-resolution Ni 2p spectrum, displayed in Fig. S24a, reveals the significant increase of the deconvoluted Ni³⁺ peak area compared to that of fresh catalysts. Besides, after a long-term OER stability test, the XPS spectrum of B 1 s confirmed the disappearance of initial M-B peak in Pd-NiFeB/NF, and there was no substantial increase of B-O peak intensity (Fig. S24d). [60] This result suggests that the NiFeB alloy component in Pd-NiFeB/NF functions as a pre-catalyst for the formation of active NiOOH. As a comparison, the operando Raman spectra of sample NiFeB/NF exhibit that only when the voltage reaches a higher level of 0.8 V, the characteristic peaks corresponding to the active species

NiOOH would then be clear, as shown in Fig. 5f, demonstrating its relatively low catalytic activity. It is thus confirmed that the introduction of Pd species in NiFeB catalyst can accelerate the formation of active NiOOH species during OER and consequently be favorable for the improvement of its catalytic activity.

Fig. 5g and Fig. S25 are the operando Raman spectra of sample Pd-NiFeB/NF and NiFeB/NF during HER. In Fig. 5g, sample Pd-NiFeB/NF displays one peak at $\sim 526 \text{ cm}^{-1}$ under the voltage of -1.4 V , which are attributed to the stretching vibration of Ni-O. Since water dissociation ($\text{H}_2\text{O} + \text{e}^- \rightarrow \text{OH}^- + \text{H}^+$, Volmer step) is the first step during HER, the resultant OH⁻ can be easily adsorbed and activated at positively charged Ni sites to form the Ni-O. Meanwhile, H⁺ is transferred to the Pd nanoclusters to form Pd-H⁺. The specific adsorption of OH⁻ and H⁺ on Ni sites and Pd centers enhances the separation of these two intermediates and accelerates the Volmer step during HER [22]. As a result, high activity is thus obtained as shown in Fig. 4g. By contrast, for NiFeB/NF catalysts, the Raman spectra of Fig. S25 show that the characteristic Ni-O peak is undetected in the testing potential range, meaning a positive contribution of Pd nanoclusters to H₂O dissociation processes. Consequently, it demonstrates a relatively low catalytic activity compared to Pd-NiFeB/NF catalysts.

3.3.2. Theoretical simulations

Density functional theory (DFT) simulations were performed to investigate the origin of enhanced HER and OER electrocatalytic activity of here synthesized Pd-NiFeB catalysts. Based on the XPS results, it can be concluded that the Pd-NiFeB catalyst predominantly consists of the amorphous NiFeB alloy phase and Pd nanoclusters, which serves as a

pre-catalyst during the catalytic reaction.[25] Thus, a theoretical model of Pd-NiFeB heterostructure was built to elucidate the interfacial charge properties based on amorphous NiFeB alloy and crystalline Pd nanoclusters. For the NiFeB amorphous alloy, the structure is constructed by molecular dynamics simulations (Fig. 6a and Fig. S26). Then, crystalline Pd as nanoclusters is loaded on the surface of amorphous NiFeB alloy to simulate Pd-NiFeB heterostructure (Fig. 6b and Fig. S26). The charge distribution and transfer were first conducted by Bader charge analysis. As shown in Fig. 6c and Fig. S27, the differential charge density image reveals that the charge redistribution of Ni sites in Pd-NiFeB heterostructure is obvious. Due to the introduction of Pd species, the extensive electron (0.408 e⁻) transfers from the Ni atoms to Pd atoms (blue and yellow colors representing the accumulation and depletion of electrons respectively). A strong electron depletion phenomenon around the Ni site promotes the production of high valence Ni species, agreeing well with above XPS results. In addition, the electron transport capability of NiFeB and Pd-NiFeB can be determined by the work function (WF). The minimum energy required for an electron escaping from the Fermi level to an infinite distance is defined as the WF (Fig. S28), and the relatively small WF represents an easy process for electron transfer [61]. As illustrated in Fig. 6d, the calculated WF of both NiFeB and Pd-NiFeB are 4.96 eV and 4.84 eV respectively, which implies that the Pd-NiFeB catalyst has a strong intrinsic driving force for electrons pumping and accumulating. Thus, the amorphous NiFeB alloy/crystalline Pd nanoclusters heterostructure improves the charge transport capability, which

effectively compensates for the sluggish charge transfer of the amorphous catalyst.

The density of states (DOS) of the theoretical models reveals the d-band center (ε_d) of NiFeB and Pd-NiFeB. According to the Hammer-Nørskov d-band model, the d-band center (ε_d) away from the Fermi level means that the interaction between the materials surface sites and the adsorbate is weak, while the ε_d close to the Fermi level implies a stronger interaction [62]. As previously reported, owing to their disordered atomic arrangement, amorphous electrocatalysts possess abundant surface defects and dangling bonds and enhanced or even excessive adsorption capability toward reaction intermediates [15]. The heterostructure construction can effectively modulate the ε_d of the amorphous catalyst, and consequently their adsorption capability [52]. As shown in Fig. 6e, the calculated ε_d of NiFeB and Pd-NiFeB are -2.07 and -2.19 eV, respectively. Noble metals-Pd interaction in NiFeB makes ε_d more negative, weakening binding strength with reaction mediates. Therefore, the ε_d of the heterostructure Pd-NiFeB catalyst is further optimized. The free energy barrier calculations will further explain in detail the reasons for the outstanding catalytic activity of Pd-NiFeB sample.

The free energies (G) of HER and OER based on the two models were calculated. First, the free energy change (ΔG) of HER processes was investigated. As shown in Fig. 6f, the ΔG_{H^*} in Pd-NiFeB is -0.034 eV after coupling the NiFeB alloy, demonstrating that an optimum ΔG_{H^*} value close to zero suggests a high HER activity. Moreover, the ΔG_{H^*} of

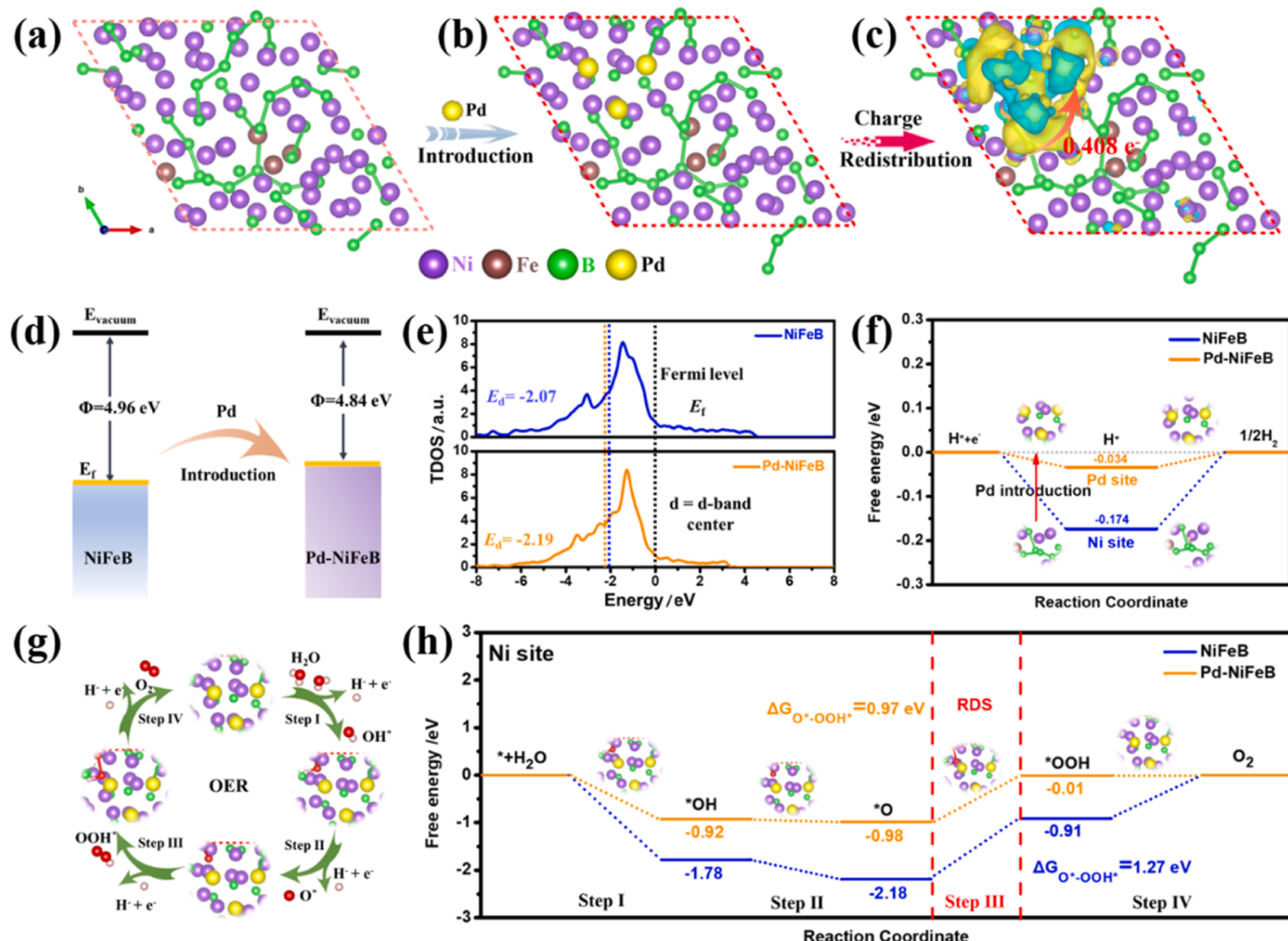


Fig. 6. Schematics of optimized models of (a) NiFeB and (b) Pd-NiFeB. (c) Differential charge densities of the Pd-NiFeB (blue region: charge accumulation, yellow region: charge depletion). (d) Work function of NiFeB and Pd-NiFeB. (e) DOS profiles of NiFeB and Pd-NiFeB. (f) Energy barriers for HER process. (g) Typical OER mechanisms of Pd-NiFeB. (h) Energy barriers for four-electron-step OER process on Ni site.

H^* adsorption in NiFeB and Pd-NiFeB is -0.174 eV and -0.034 eV, demonstrating that the HER activity of NiFeB can be improved after the integration of crystalline Pd nanoclusters. To further explore the mechanism of OER activity for Pd-NiFeB, the G of the three oxygen-based intermediates (*OH , *O , and *OOH) in the OER mechanism was calculated during the OER process. Fig. 6g reveals the adsorption of *OH , *O , and *OOH onto the Ni bridge site. As shown in Fig. 6h, in NiFeB, the energy barrier of the elementary reaction $^*O \rightarrow ^*OOH$ ($\Delta G_{^*O \rightarrow ^*OOH}$) is 1.27 eV, which is higher than those of the other three elementary steps ($H_2O^* \rightarrow HO^*$ (1.78 eV), $HO^* \rightarrow O^*$ (0.4 eV) and $HOO^* \rightarrow O_2$ (0.91 eV)), illustrating that this step is the rate-determining step (RDS) of OER. After the integration of crystalline Pd nanoclusters, the $\Delta G_{^*O \rightarrow ^*OOH}$ for Pd-NiFeB is 0.97 eV, which is much lower than that of NiFeB. This result emphasizes the significant contribution of crystalline Pd nanoclusters to optimizing the RDS of water oxidation, which is in agreement with the OER activity obtained in Fig. 4a.

4. Conclusion

In summary, we herein report a one-step electroless plating strategy to synthesize amorphous NiFeB alloy-crystalline Pd nanocluster heterostructure electrocatalyst. The comprehensive structure characterizations confirm the formation of heterostructures in sample Pd-NiFeB/NF. Simultaneously, the introduction of crystalline Pd nanoclusters can significantly optimize the electronic structures and promote electron transfer, further contributing to its outstanding electrocatalytic performances. Notably, the assembled Pd-NiFeB/NF//Pd-NiFeB/NF electrolyzer requires a low cell voltage of 1.81 V to deliver a current density of 500 mA cm^{-2} highly durably for at least 100 h in a 1.0 M KOH solution. DFT results confirm the reduction of the energy barrier owing to the charge redistribution from Ni atoms to Pd atoms in Pd-NiFeB materials. This work provides a facile one-step strategy to construct high-performance heterostructure electrocatalysts for understanding in-depth the effects of amorphous-crystalline heterostructure on catalytic activity.

CRediT authorship contribution statement

Bowen Lu: Writing – original draft, Writing – review & editing, Conceptualization, Methodology, Formal analysis, Investigation, Supervision. **Rongmin Dun:** Resources, Investigation. **Wei Wang:** Supervision. **Jian Huang:** Resources, Investigation. **Jingxian Wu:** Investigation. **Zi Le Hua:** Writing – original draft, Writing – review & editing, Conceptualization, Funding acquisition. **Jianlin Shi:** Writing – original draft, Funding acquisition.

Declaration of Competing Interest

The authors declare the following financial interests/personal relationships which may be considered as potential competing interests: Zi Le Hua reports financial support was provided by Shanghai Institute of Ceramics Chinese Academy of Sciences. Zi Le Hua reports a relationship with Shanghai Institute of Ceramics Chinese Academy of Sciences that includes: employment. The authors declare that they have no known competing financial interests or personal relationships that could have appeared to influence the work reported in this paper.

Data Availability

The authors are unable or have chosen not to specify which data has been used.

Acknowledgements

This work was financially supported by the National Natural Science Foundation of China (grand No: 21776297, 21878116, and U1510107).

Appendix A. Supporting information

Supplementary data associated with this article can be found in the online version at doi:10.1016/j.apcatb.2023.123343.

References

- [1] J. Fan, C. Fu, R. Liang, Mild construction of "midas touch" metal-organic framework-based catalytic electrodes for highly efficient overall seawater splitting, *Small* 18 (2022), e2203588.
- [2] G. Fu, X. Kang, Y. Zhang, Coordination effect-promoted durable Ni(OH)₂ for energy-saving hydrogen evolution from water/methanol Co-electrocatalysis, *Nanomicro Lett.* 14 (2022) 200.
- [3] J. Jiang, M. Wang, W. Yan, Highly active and durable electrocatalytic water oxidation by a Ni_{0.45}/NiO core-shell heterostructured nanoparticulate film, *Nano Energy* 38 (2017) 175–184.
- [4] X. Liu, J. Huang, T. Li, High-efficiency oxygen evolution catalyzed by Sn-Co-Ni phosphide with oriented crystal phases, *J. Mater. Chem. A* 10 (2022) 13448–13455.
- [5] Y. Wu, Y. Liu, G.-D. Li, Efficient electrocatalysis of overall water splitting by ultrasmall Ni_xCo_{3-x}S₄ coupled Ni₃S₂ nanosheet arrays, *Nano Energy* 35 (2017) 161–170.
- [6] J. Yuan, X. Cheng, H. Wang, A. Superaerophobic, Bimetallic selenides heterostructure for efficient industrial-level oxygen evolution at ultra-high current densities, *Nanomicro Lett.* 12 (2020) 104.
- [7] Y. Jia, T.-H. Huang, S. Lin, Stable Pd–Cu hydride catalyst for efficient hydrogen evolution, *Nano Lett.* 22 (2022) 1391–1397.
- [8] D.K. Bediako, B. Lassalle-Kaiser, Y. Surendranath, Structure-activity correlations in a nickel-borate oxygen evolution catalyst, *J. Am. Chem. Soc.* 134 (2012) 6801–6809.
- [9] J. Chang, Q. Lv, G. Li, J. Ge, C. Liu, W. Xing, Core-shell structured Ni₁₂P₅/Ni₃(PO₄)₂ hollow spheres as difunctional and efficient electrocatalysts for overall water electrolysis, *Appl. Catal. B* 204 (2017) 486–496.
- [10] M. Karatok, H.T. Ngan, X. Jia, C.R. O'Connor, J.A. Boscoboinik, D.J. Stacchiola, P. Sautet, R.J. Madix, Achieving ultra-high selectivity to hydrogen production from formic acid on Pd-Ag alloys, *J. Am. Chem. Soc.* 145 (2023) 5114–5124.
- [11] A. Chunduri, S. Gupta, O. Bapat, A. Bhide, R. Fernandes, M.K. Patel, V. Bambole, A. Miottello, N. Patel, A unique amorphous cobalt-phosphide-boride bifunctional electrocatalyst for enhanced alkaline water-splitting, *Appl. Catal. B* 259 (2019), 118051.
- [12] Y. Zhou, H.J. Fan, Progress and challenge of amorphous catalysts for electrochemical water splitting, *ACS Mater. Lett.* 3 (2020) 136–147.
- [13] H. Han, H. Choi, S. Mhin, Advantageous crystalline-amorphous phase boundary for enhanced electrochemical water oxidation, *Energy Environ. Sci.* 12 (2019) 2443–2454.
- [14] D. Li, Y. Qin, J. Liu, Dense crystalline-amorphous interfacial sites for enhanced electrocatalytic oxygen evolution, *Adv. Funct. Mater.* 32 (2021), 2107056.
- [15] M. Wang, J. Ma, K. Lu, Advances in ambient selective electrohydrogenation of nitrogen to ammonia: strategies to strengthen nitrogen chemisorption, *J. Mater. Chem. A* 11 (2023), 3871–388.
- [16] W. He, R. Zhang, D. Cao, Y. Li, J. Zhang, Q. Hao, H. Liu, J. Zhao, H.L. Xin, Super-hydrophilic microporous Ni(OH)_x/Ni₃S₂ heterostructure electrocatalyst for large-current-density hydrogen evolution, *Small* 19 (2023), e2205719.
- [17] K. Dastafkan, X. Shen, R.K. Hocking, Q. Meyer, C. Zhao, Monometallic interphasic synergy via nano-hetero-interfacing for hydrogen evolution in alkaline electrolytes, *Nat. Commun.* 14 (2023) 547.
- [18] Y.J. Son, K. Kawashima, B.R. Wygant, Anodized nickel foam for oxygen evolution reaction in Fe-free and unpurified alkaline electrolytes at high current densities, *ACS Nano* 15 (2021) 3468–3480.
- [19] J. Chi, H. Yu, G. Jiang, J. Jia, B. Qin, B. Yi, Z. Shao, Construction of orderly hierarchical FeOOH/NiFe layered double hydroxides supported on cobaltous carbonate hydroxide nanowire arrays for a highly efficient oxygen evolution reaction, *J. Mater. Chem. A* 6 (2018) 3397–3401.
- [20] Y. Nagai, K. Dohmae, Y. Ikeda, In situ redispersion of platinum autoexhaust catalysts: an on-line approach to increasing catalyst lifetimes? *Angew. Chem. Int. Ed.* 47 (2008) 9303–9306.
- [21] H. Xie, S. Chen, J. Liang, T. Wang, Z. Hou, H.L. Wang, G. Chai, Q. Li, Weakening intermediate bindings on CuPd/Pd core/shell nanoparticles to achieve Pt-like bifunctional activity for hydrogen evolution and oxygen reduction reactions, *Adv. Funct. Mater.* 31 (2021), 2100883.
- [22] A. Pei, G. Li, L. Zhu, Z. Huang, J. Ye, Y.C. Chang, S.M. Osman, C.W. Pao, Q. Gao, B. H. Chen, R. Luque, Nickel hydroxide-supported Ru single atoms and Pd nanoclusters for enhanced electrocatalytic hydrogen evolution and ethanol oxidation, *Adv. Funct. Mater.* 32 (2022), 2208587.
- [23] Y. Jia, T.H. Huang, S. Lin, L. Guo, Y.M. Yu, J.H. Wang, K.W. Wang, S. Dai, Stable Pd–Cu hydride catalyst for efficient hydrogen evolution, *Nano Lett.* 22 (2022) 1391–1397.
- [24] C. Qiang, L. Zhang, H. He, Y. Liu, Y. Zhao, T. Sheng, S. Liu, X. Wu, Z. Fang, Efficient electrocatalytic water splitting by bimetallic cobalt iron boride nanoparticles with controlled electronic structure, *J. Colloid Interface Sci.* 604 (2021) 650–659.
- [25] Q. Wang, Z. Jia, J. Li, Y. He, Y. Yang, Y. Li, L. Sun, B. Shen, Attractive electron delocalization behavior of FeCoMoPB amorphous nanoparticles for highly efficient alkaline water oxidation, *Small* 18 (2022), e2204135.

[26] S.-W. Wu, S.-Q. Liu, X.-H. Tan, W.-Y. Zhang, K. Cadien, Z. Li, Ni₃S₂-embedded NiFe LDH porous nanosheets with abundant heterointerfaces for high-current water electrolysis, *Chem. Eng. Eng.* **442** (2022), 136105.

[27] S.M.A. Shibli, A.H. Riyas, M. Ameen Sha, R. Mole, Tuning of phosphorus content and electrocatalytic character of CeO₂-RuO₂ composite incorporated Ni-P coating for hydrogen evolution reaction, *J. Alloy. Compd.* **696** (2017) 595–603.

[28] M. Moloudi, A. Noori, M.S. Rahmanifar, Layered double hydroxide templated synthesis of amorphous NiCoFeB as a multifunctional electrocatalyst for overall water splitting and rechargeable zinc–air batteries, *Adv. Energy Mater.* **13** (2022), 2203002.

[29] H.-I. Li, Y.-y Wang, C.-m Liu, S.-m Zhang, H.-f Zhang, Z.-w Zhu, Enhanced OER performance of NiFeB amorphous alloys by surface self-reconstruction, *Int. J. Hydrog. Energy* **47** (2022) 20718–20728.

[30] P. Zhang, M. Wang, Y. Yang, T. Yao, H. Han, L. Sun, Electroless plated Ni–B films as highly active electrocatalysts for hydrogen production from water over a wide pH range, *Nano Energy* **19** (2016) 98–107.

[31] H. Liao, G. Ni, P. Tan, Y. Liu, K. Chen, G. Wang, M. Liu, J. Pan, Borate narrowed band gap of nickel–iron layer double hydroxide to mediate rapid reconstruction kinetics for water oxidation, *Appl. Catal. B* **317** (2022), 121713.

[32] Y. Bai, Y. Wu, X. Zhou, Y. Ye, K. Nie, J. Wang, M. Xie, Z. Zhang, Z. Liu, T. Cheng, C. Gao, Promoting nickel oxidation state transitions in single-layer NiFeB hydroxide nanosheets for efficient oxygen evolution, *Nat. Commun.* **13** (2022) 6094.

[33] V.H. Do, P. Prabhu, V. Jose, T. Yoshida, Y. Zhou, H. Miwa, T. Kaneko, T. Uruga, Y. Iwasawa, J.M. Lee, Pd–PdO nanodomains on amorphous Ru metathene oxide for high-performance multifunctional electrocatalysis, *Adv. Mater.* **35** (2023), e2208860.

[34] A. Doménech-Carbó, E. Coronado, P. Díaz, A. Ribera, Solid-state electrochemical method for determining core and shell size in Pd@PdO nanoparticles, *Electroanalysis* **22** (2010) 293–302.

[35] L. Trottochaud, S.L. Young, J.K. Ranney, S.W. Boettcher, Nickel–iron oxyhydroxide oxygen-evolution electrocatalysts: the role of intentional and incidental iron incorporation, *J. Am. Chem. Soc.* **136** (2014) 6744–6753.

[36] Y. Wang, G. Qian, Q. Xu, H. Zhang, F. Shen, L. Luo, S. Yin, Industrially promising IrNi–FeNi₃ hybrid nanosheets for overall water splitting catalysis at large current density, *Appl. Catal. B* **286** (2021), 119881.

[37] F. Shen, Y. Wang, G. Qian, W. Chen, W. Jiang, L. Luo, S. Yin, Bimetallic iron–iridium alloy nanoparticles supported on nickel foam as highly efficient and stable catalyst for overall water splitting at large current density, *Appl. Catal. B* **278** (2020), 119327.

[38] W. Zhang, X. Jiang, Z. Dong, J. Wang, N. Zhang, J. Liu, G.R. Xu, L. Wang, Porous Pd/NiFeO_x nanosheets enhance the pH-universal overall water splitting, *Adv. Funct. Mater.* **31** (2021), 2107181.

[39] J. Wu, Z. Nie, R. Xie, X. Hu, Y. Yu, N. Yang, Self-assembled Pt–CoFe layered double hydroxides for efficient alkaline water/seawater splitting by spontaneous redox synthesis, *J. Power Sources* **532** (2022), 231353.

[40] H. Liu, Q. Jia, S. Huang, L. Yang, S. Wang, L. Zheng, D. Cao, Ultra-small Ru nanoparticles embedded on Fe–Ni(OH)₂ nanosheets for efficient water splitting at a large current density with long-term stability of 680 h, *J. Mater. Chem. A* **10** (2022) 4817–4824.

[41] T. Cui, X. Zhai, L. Guo, J.-Q. Chi, Y. Zhang, J. Zhu, X. Sun, L. Wang, Controllable synthesis of a self-assembled ultralow Ru, Ni-doped Fe₂O₃ lily as a bifunctional electrocatalyst for large-current-density alkaline seawater electrolysis, *Chin. J. Catal.* **43** (2022) 2202–2211.

[42] L. Wu, L. Yu, Q. Zhu, B. McElhenny, F. Zhang, C. Wu, X. Xing, J. Bao, S. Chen, Z. Ren, Boron-modified cobalt iron layered double hydroxides for high efficiency seawater oxidation, *Nano Energy* **83** (2021), 105838.

[43] D. Wu, B. Liu, R. Li, D. Chen, W. Zeng, H. Zhao, Y. Yao, R. Qin, J. Yu, L. Chen, J. Zhang, B. Li, S. Mu, Fe-regulated amorphous-crystal Ni(Fe)P₂ nanosheets coupled with Ru powerfully drive seawater splitting at large current density, *Small* **19** (2023), 2300030.

[44] H. Liu, X. Li, L. Chen, X. Zhu, P. Dong, M.O.L. Chee, M. Ye, Y. Guo, J. Shen, Monolithic Ni–Mo–B bifunctional electrode for large current water splitting, *Adv. Funct. Mater.* **32** (2021), 2107308.

[45] J. Fan, C. Fu, R. Liang, H. Lv, C. Fang, Y. Guo, W. Hao, Mild construction of “midas touch” metal–organic framework-based catalytic electrodes for highly efficient overall seawater splitting, *Small* **18** (2022), 2203588.

[46] S. Wei, X. Cui, Y. Xu, B. Shang, Q. Zhang, L. Gu, X. Fan, L. Zheng, C. Hou, H. Huang, S. Wen, W. Zheng, Iridium-triggered phase transition of MoS₂ nanosheets boosts overall water splitting in alkaline media, *ACS Energy Lett.* **4** (2018) 368–374.

[47] A. Pandey, A. Mukherjee, S. Chakrabarty, D. Chanda, S. Basu, Interface engineering of an RGO/MoS₂/Pd 2D heterostructure for electrocatalytic overall water splitting in alkaline medium, *ACS Appl. Mater. Interfaces* **11** (2019) 42094–42103.

[48] B. Ye, L. Huang, Y. Hou, R. Jiang, L. Sun, Z. Yu, B. Zhang, Y. Huang, Y. Zhang, Pt (111) quantum dot decorated flower-like αFe₂O₃ (104) thin film nanosheets as a highly efficient bifunctional electrocatalyst for overall water splitting, *J. Mater. Chem. A* **7** (2019) 11379–11386.

[49] B. Ye, R. Jiang, Z. Yu, Y. Hou, J. Huang, B. Zhang, Y. Huang, Y. Zhang, R. Zhang, Pt (1 1 1) quantum dot engineered Fe-MOF nanosheet arrays with porous core-shell as an electrocatalyst for efficient overall water splitting, *J. Catal.* **380** (2019) 307–317.

[50] N. Logeshwaran, S. Ramakrishnan, An efficient and durable trifunctional electrocatalyst for zinc–air batteries driven overall water splitting, *Appl. Catal. B* **297** (2021), 120405.

[51] H. Zhang, Q. Jiang, J.H.L. Hadden, F. Xie, D.J. Riley, Pd ion-exchange and ammonia etching of a Prussian blue analogue to produce a high-performance water-splitting catalyst, *Adv. Funct. Mater.* **31** (2020), 2008989.

[52] J. Zhu, R. Lu, S. Mu, Crystalline–amorphous heterostructures with assortative strong–weak adsorption pairs enable extremely high water oxidation capability toward multi-scenario water electrolysis, *Nano Energy* **110** (2023), 108349.

[53] Z. Lyu, X. Zhang, X. Liao, K. Liu, H. Huang, J. Cai, Q. Kuang, Z. Xie, S. Xie, Two-dimensionally assembled Pd–Pt–Ir supernanosheets with subnanometer interlayer spacings toward high-efficiency and durable water splitting, *ACS Catal.* **12** (2022) 5305–5315.

[54] J. Li, C. Hou, C. Chen, W. Ma, Q. Li, L. Hu, X. Lv, J. Dang, Collaborative interface optimization strategy guided ultrafine RuCo and MXene heterostructure electrocatalysts for efficient overall water splitting, *ACS Nano* **17** (2023) 10947–10957.

[55] X. Ding, Y. Xia, Q. Li, S. Dong, X. Jiao, D. Chen, Interface engineering of Co(OH)₂/Ag/FeP hierarchical superstructure as efficient and robust electrocatalyst for overall water splitting, *ACS Appl. Mater. Interfaces* **11** (2019) 7936–7945.

[56] Y. Li, Y.-C. Miao, C. Yang, Y.-X. Chang, Y. Su, H. Yan, S. Xu, Ir nanodots decorated Ni3Fe nanoparticles for boosting electrocatalytic water splitting, *Chem. Eng. J.* **451** (2023), 138548.

[57] D. Liu, Z. Song, S. Cheng, Y. Wang, A. Saad, S. Deng, J. Shen, X. Huang, X. Cai, P. Tsiaikaras, Mesoporous IrNiTa metal glass ribbon as a superior self-standing bifunctional catalyst for water electrolysis, *Chem. Eng. J.* **431** (2022), 134210.

[58] H. Liu, J. Cheng, W. He, Y. Li, J. Mao, X. Zheng, C. Chen, C. Cui, Q. Hao, Interfacial electronic modulation of Ni₃S₂ nanosheet arrays decorated with Au nanoparticles boosts overall water splitting, *Appl. Catal. B* **304** (2022), 120935.

[59] W.H. Lai, L.F. Zhang, W.B. Hua, General π-electron-assisted strategy for Ir, Pt, Ru, Pd, Fe, Ni single-atom electrocatalysts with bifunctional active sites for highly efficient water splitting, *Angew. Chem. Int. Ed.* **58** (2019) 11868–11873.

[60] W. Hao, D. Yao, Q. Xu, R. Wang, C. Zhang, Y. Guo, R. Sun, M. Huang, Z. Chen, Highly efficient overall-water splitting enabled via grafting boron-inserted Fe–Ni solid solution nanosheets onto unconventional skeleton, *Appl. Catal. B* **292** (2021), 120188.

[61] D. Chen, R. Lu, R. Yu, Work-function-induced interfacial built-in electric fields in Os–OsSe₂ heterostructures for active acidic and alkaline hydrogen, *Evolv. Angew. Chem. Int. Ed.* **61** (2022), e202208642.

[62] Y. Zhang, Z. Zeng, D. Ho, D-band center optimization of iron carbide via Cr substitution for enhanced alkaline hydrogen evolution, *Mater. Today Energy* **29** (2022), 101133.